



Fatigue strength improvement due to alloying steel weld toes with WC tool constituent elements through friction stir processing

Hajime Yamamoto¹ · Shodai Koga¹ · Kazuhiro Ito¹ · Yoshiki Mikami¹

Received: 4 October 2021 / Accepted: 5 January 2022 / Published online: 19 January 2022
© The Author(s) 2022

Abstract

Friction stir processing (FSP) enables surface modifications can likely be applied as a new post-weld treatment for improving fatigue strength. When applying FSP to high-strength materials, tool wear occurring at the interface between the tool tip and the topmost steel layer has been regarded as an unavoidable issue and is related to the tool rotational speed. The present study investigated the relationship between the tool rotational speed and fatigue strength of arc-welded high-strength low-alloy (HSLA) steel joints with weld toes subjected to FSP using a spherical-tip WC tool. FSP was conducted on the weld toe of HSLA steel joints with various tool rotational speeds. Tool wear increased with increase in tool rotational speed, and consequently contents of constituent elements of the WC tool increased in the topmost steel layer of weld toes, leading to large increase in fatigue strength. One reason for the increase with tool rotational speed is significant increase in solid solution hardening due to supersaturated W and C in the topmost steel layer consisting of martensite laths. The hardened topmost steel layer prevented fatigue crack initiation, and the increased fatigue strength depended on the contents of supersaturated W and C. Alloying of the topmost steel layer with tool constituent elements of W and C accompanied with WC tool wear during FSP is unique additive manufacturing to increase the fatigue strength of welded joints, and can be employed locally on structural components susceptible to fatigue.

Keywords Friction stir processing · Tool wear · Alloying · Fatigue strength · Post-weld treatment · High-strength low-alloy steel

1 Introduction

Fatigue strength of arc-welded joints is commonly said to be lower than that of the base metal, because of stress concentration, tensile residual stress, and deterioration of the mechanical properties due to microstructural change at the weld toe. Various post-weld treatments have been proposed to increase fatigue strength of the welds, and are generally divided into two groups of residual stress modification, those of peening [1–4] and post-weld heat treatment [5, 6], and weld geometry modification such as grinding [7–9] and remelting [10–12]. Residual stress modification is more effective than weld geometry modification under low applied stress amplitude, but seems not effective under high applied stress amplitude, because of residual stress relaxation during fatigue [13]. On

the other hand, fatigue strength and life increased by reducing stress concentration at the weld toe, and independently of the applied stress amplitude. In addition, remelting the weld toe using arc plasma or laser as a heat source led not only to smoothing of the weld surface profile, but also to removal of internal defects, including cracks, without reducing plate thickness [11]. However, it has been reported that remelting by means such as tungsten inert gas dressing caused softening around the remelted zone, which disturbed large improvement of fatigue strength of the high-strength steel welds [12].

On the other hand, we reported that friction stir processing (FSP) significantly increased the fatigue strength of arc-welded steel joints [14–18] and can likely be used as a new post-weld treatment. FSP is a surface modification technique using a rotational tool, based on the principle of friction stir welding (FSW) [19]. The stir zone (SZ) produced locally by FSP can consist of fine homogeneous microstructure, resulting in mechanical properties superior to those of the base metal [20–23]. In addition, material flow during FSP contributes to elimination of internal defects and refinement of

✉ Hajime Yamamoto
h.yamamoto@jwri.osaka-u.ac.jp

¹ Joining and Welding Research Institute, Osaka University,
11-1 Mihogaoka, Ibaraki, Osaka 567-0047, Japan

coarse precipitates, which can become crack initiation sites, resulting in the improvement of fatigue properties of cast alloys [24–26]. Considering these advantages, Costa et al. also reported that FSP on the weld toes increased fatigue strength of several aluminum alloy joints fabricated by metal inert gas welding [27–30].

Among the papers mentioned above, we demonstrated the fatigue strength improvement of arc-welded high-strength low-alloy (HSLA) steel joints with weld toes that had been subjected to FSP using a spherical-tip WC tool [17]. That was the first paper regarding alloying the topmost steel layer of the weld toes with W and C, which are constituent elements of the WC tool, accompanied with the tool wear during FSP. The supersaturated W and C caused significant solid solution hardening in the topmost steel layer of the weld toes and contributed to the improvement of the fatigue strength. The alloying is the newest unique additive manufacturing technique accompanied with tool wear during FSP to increase the fatigue strength of welded joints, and can be employed locally on structural components susceptible to fatigue (e.g., automobile components). Importantly, the results indicated positive utilization of the tool wear during FSP as a new line of thought, as the tool wear has been considered as an unavoidable issue in FSW/FSP of high-strength materials.

However, the relationship between the fatigue strength increase and tool rotational speed related to contents of the supersaturated W and C was not systematically shown in the previous study [17], which focused only on the applicability of FSP to the steel weld toe. We therefore intended to clarify influence of the tool rotational speed on improving fatigue strength. Increase in the tool rotational speed would increase the WC tool wear, occurring at the interface between the tool tip and a topmost steel layer, leading to increasing contents of constituent elements of the WC tool in the topmost steel layer of weld toes. This would increase solid solution hardening and consequently increase fatigue strength. In the present study, the relationship between the tool rotational speed and fatigue strength of arc-welded HSLA steel joints with weld toes subjected to FSP using a spherical-tip WC tool was investigated.

2 Experimental procedures

HSLA steel plates of 10-mm thickness and filler metals were prepared, with the chemical compositions as shown in Table 1. Three-pass CO₂ gas-shielded arc welding was

conducted in V-groove with a root gap of 5 mm and angle of 60° in accordance with the conditions shown in Table 2. FSP was conducted on weld toes of the obtained butt-welded HSLA steel joints using a spherical-tip WC tool. The tool, having a 15-mm-diameter spherical tip with a curvature radius of 10 mm as shown in Fig. 1(a), was made of WC particles (88–91 mass%) with a size range of about 2–4 μm and Ni-based binder. FSP was conducted at positions 2 mm away from the right and left ends of the weld toe for the prevention of flash formation [17]. The positions corresponded to the tool rotational axis (Fig. 1(b)). The tool was tilted backward 3° and operated at a travel speed of 100 mm/min along the weld bead and downward force of 18.3 kN with various rotational speeds of 400–1000 rpm (Fig. 1(c)). The advancing side (AS) and retreating side (RS) during FSP corresponded to the excess weld metal and base metal positions, respectively.

Cross-sectional images of the weld toes with and without FSP were taken using an optical microscope (OM) (VHX-7000, Keyence Co., Japan) and a scanning electron microscope (SEM) (SU-70, Hitachi High-Tech Co., Japan). Specimens with mirror-polished surfaces for cross-sectional images were etched with 2 vol% nital solution. Major elements in both the steel and the tool were analyzed using an electron probe micro-analyzer (EPMA) (JXA-8530F, JEOL Co., Japan). To obtain a high-magnification image of a nanoscale area in the weld toe after FSP, thin film specimens were taken from the specimens to obtain cross-sectional images using a focused ion beam machining device (JIB-4500, JEOL Co., Japan). Microstructure observation and elemental analysis of the obtained thin film specimens were conducted using a transmission electron microscope (TEM) (JEM-2010F, JEOL Co., Japan) equipped with an energy dispersive X-ray spectroscopy (EDS). Vickers hardness tests (HM-221, Mitutoyo Co., Japan) were carried out at room temperature with an applied load of 49 mN and loading time of 15 s.

Four-point bending fatigue tests (EFH-50-5-5, Saginomiya Co., Japan) were carried out at room temperature with a sinusoidal waveform of 20 Hz as a function of maximum applied stress with a stress ratio of 0.1. Specimens with welds at the center (145 mm long × 10 mm wide × 10 mm thick) were prepared by cutting the butt-welded steel plates with and without FSP using an electrical discharge machine (AG360L, Sodick Co., Japan). Outer and inner spans of 10-mm-diameter pins were 90 and 50 mm, respectively. The weld bead was located at the center of the inner span, and

Table 1 Chemical compositions of the base and filler metals (mass%)

Material	C	Si	Mn	P	S	Cu	Ni	Cr	Mo	V	Al	Fe
Base metal (HSLA steel)	0.14	0.23	1.08	0.014	0.006	0.01	0.01	0.02	-	0.002	0.028	Bal
Filler metal	0.03	0.55	1.55	0.011	0.007	0.02	0.01	0.02	<0.01	<0.01	-	Bal

Table 2 CO₂ gas-shielded arc welding parameters

Pass	Welding current, <i>I</i> (A)	Arc voltage, <i>V</i> (V)	Welding speed, <i>v</i> (mm/min)	Torch drag angle, <i>θ</i> (°)
1st	170	22	130	-
2nd	280	32	200	-
3rd	280	29	300	5

the base metals on both right and left sides of the weld bead were included between inner-span pins. To characterize the fracture location and crack initiation site, the cross section and fracture surface of the specimen after the fatigue test were observed by OM and SEM. To characterize the local fatigue strength of the topmost steel layer at the weld toe modified by FSP, small flat tensile specimens with a dumb-bell shape (gauge length of 1 mm, gauge width of 0.5 mm, 5-mm square gripped ends, and thickness of 0.5 mm) were taken from the topmost layer of the weld toe with and without FSP, and tensile tests (EZ Graph, Shimadzu Co., Japan) were conducted at room temperature at a strain rate of $1.0 \times 10^{-3} \text{ s}^{-1}$.

3 Results and discussion

3.1 Microstructural characterization of weld toes

Figure 2 shows cross-sectional OM images of the as-welded joint. Typical weld toe radius and angle were measured to be about 0.27 mm and 27°, respectively (Fig. 1(b)). The base metal and weld toe consisted of banded ferrite/pearlite structure (Fig. 2(c), (d)) and coarse bainitic ferrite grains (Fig. 2(e), (f)).

FSP was conducted on the weld toe surfaces to improve fatigue strength of the butt-welded joints. Figure 3 shows cross-sectional OM and SEM images of the weld toes with

FSP at the tool rotational speeds of 400, 600, 800, and 1000 rpm (hereafter, samples FSP400, FSP600, FSP800, and FSP1000, respectively). FSP changed weld toe geometry due to plastic deformation, in addition to formation of the SZ. The weld toe radius was significantly increased to about 3.69, 2.65, 3.53, and 3.79 mm in samples FSP400, FSP600, FSP800, and FSP1000, respectively, but with slightly higher weld toe angles (Fig. 3(a)–(d)) in comparison to that of the as-welded toe (Fig. 2(b)). These macroscopic changes did not seem to depend on tool rotational speed. On the other hand, a surface morphological and microstructural feature of the topmost layer of the weld toes after FSP varied with tool rotational speed: a notched surface was observed in FSP400 (Fig. 3(e)), while smooth surfaces were observed in FSP600, FSP800, and FSP1000 (Fig. 3(f)–(h)). The notched surface in FSP400 can be attributed to materials having been removed at the front of the tool and subsequently accumulating behind the tool. The FSP condition of 400 rpm was not appropriate for sound surface modification on the weld toe. In microstructure of the topmost layer including the SZ, there was an obvious difference in addition to significant grain refinement in all weld toes with FSP. In the OM images for FSP800 and FSP1000 (Fig. 3(g), (h)), discontinuous and continuous areas with white contrast were observed at the outermost surface layer, in comparison to those for FSP400 and FSP600 (Fig. 3(e), (f)). The white contrast areas correspond to the portions alloyed with constituent elements of the WC tool, and the thicker portion for FSP1000 was provided by the faster tool rotational speed. This suggests that the tool wear amount increased with increasing tool rotational speed. To characterize microstructure of the topmost layer at the weld toe, the specimen surface was etched with 2 vol% nital solution, and cross-sectional SEM images of the outermost surface layer and a layer around 100 μm below the surface were obtained, as shown in Fig. 3(i)–(l) and (m)–(p), respectively. Fine

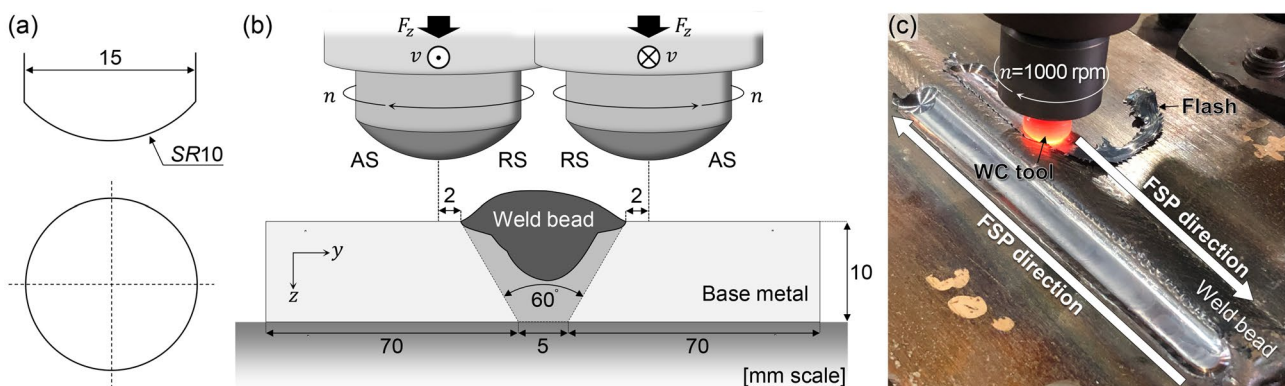


Fig. 1 Schematic illustrations of (a) a tool shape and (b) arrangement of the tool and a weld toe during FSP. (c) A photo image of a typical FSP operation with the tool rotational speed of 1000 rpm

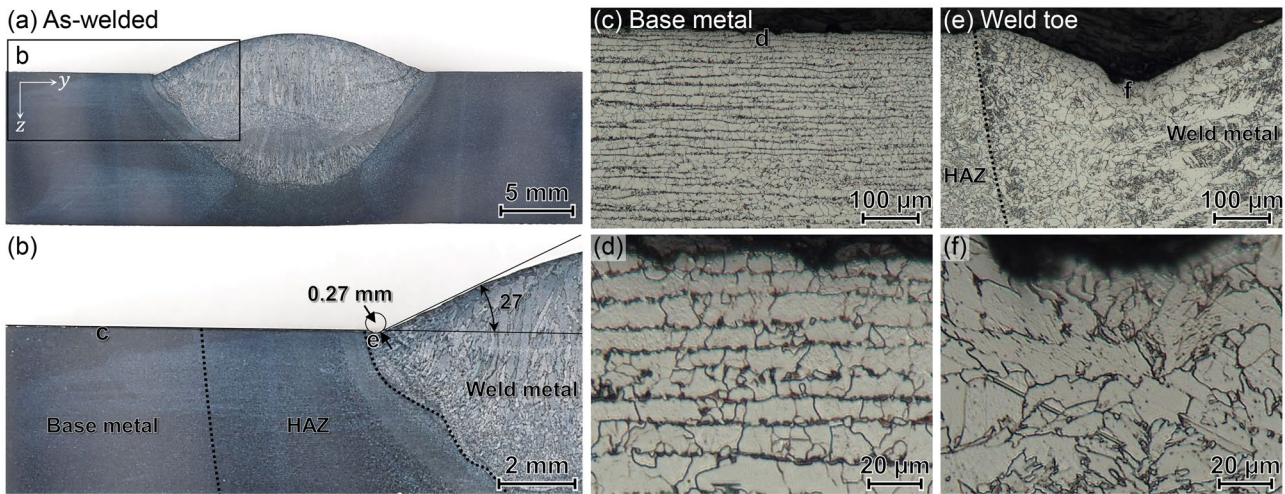


Fig. 2 (a) Cross-sectional OM image of the whole weld in an as-welded joint and (b) enlargement of rectangular frame in (a). (c and d) Cross-sectional OM images of typical base metal portions and (e and f) typical weld toe portions in (a)

equiaxed polygonal ferrite grains were observed in both layers mainly in FSP400 and FSP600 (Fig. 3(i), (j), (m), (n)). The volume fraction of bainitic ferrite grains increased with increasing tool rotational speed in the layer

100 μm below the surface, suggesting that the peak temperature during FSP was beyond the phase transformation temperature and the volume fraction of transformed austenite grains increased. The layer eventually showed a

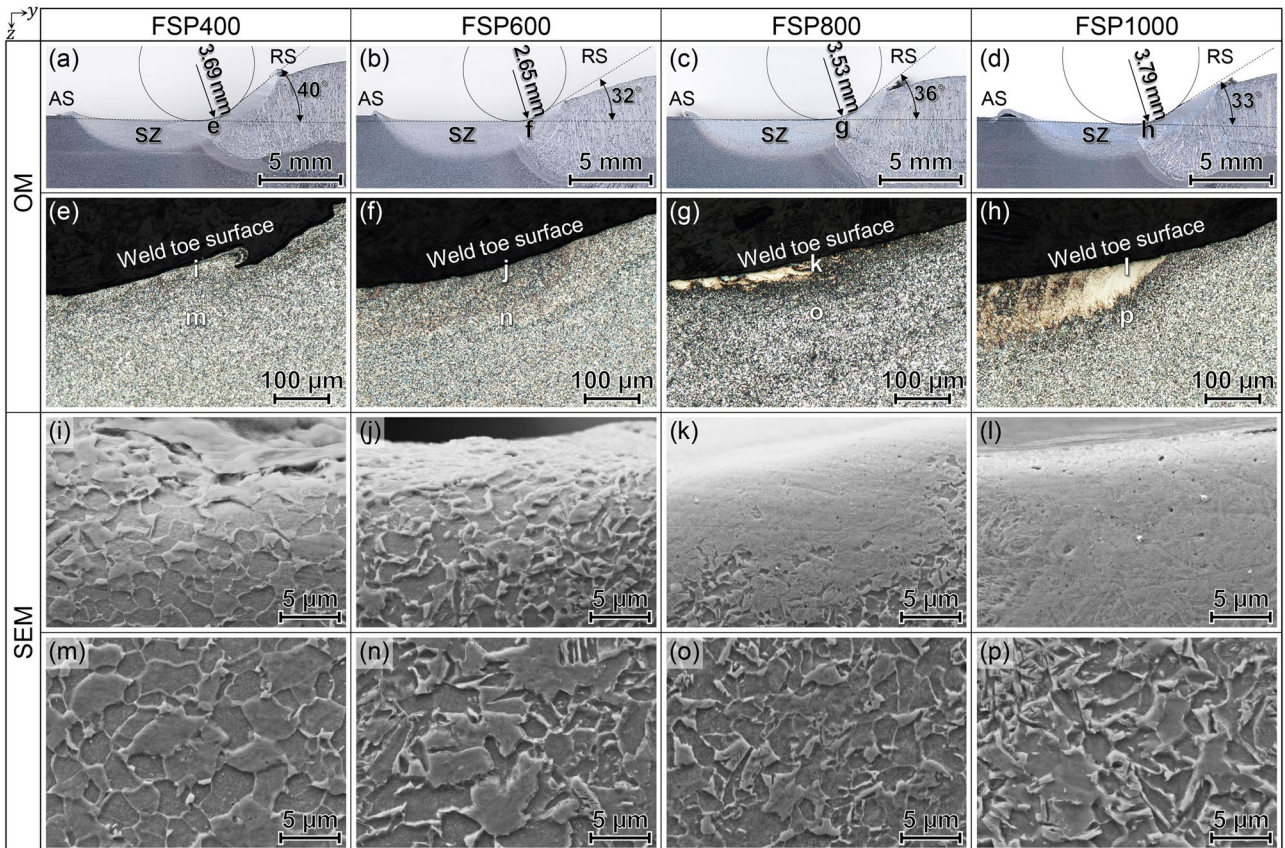


Fig. 3 Cross-sectional OM images of weld toes in samples (a and e) FSP400, (b and f) FSP600, (c and g) FSP800, and (d and h) FSP1000 and (i–p) SEM enlargements of positions i and m in (e), j and n in (f), k and o in (g), and l and p in (h)

fully bainitic structure in FSP1000 (Fig. 3(p)). This indicates that the peak temperature during FSP exceeded the A_{C3} point with the fully austenite transformation. The bainitic ferrite grains arose through transformation from the austenite phase during cooling in FSP, while polygonal ferrite grains arose through dynamic recrystallization during FSP. The outermost surface layer having smooth continuity formed in FSP800 and FSP1000 is considered to contain tool constituent elements of W and C, as explained in a previous study [31], as shown in Fig. 3(k) and (i). This suggests that the layer consisted of fully martensite structure with ultrafine laths.

To identify the elemental contents and their influence on the hardness in the outermost surface layer, EPMA and Vickers hardness tests were conducted. Figure 4 shows relationship between increment in W and C contents and hardness with respect to depth from the weld toe surface. The increment was estimated by subtracting the average content obtained in the topmost layer of the as-welded toe from the content measured using EPMA. Increment in the contents of W and C derived from the tool are associated

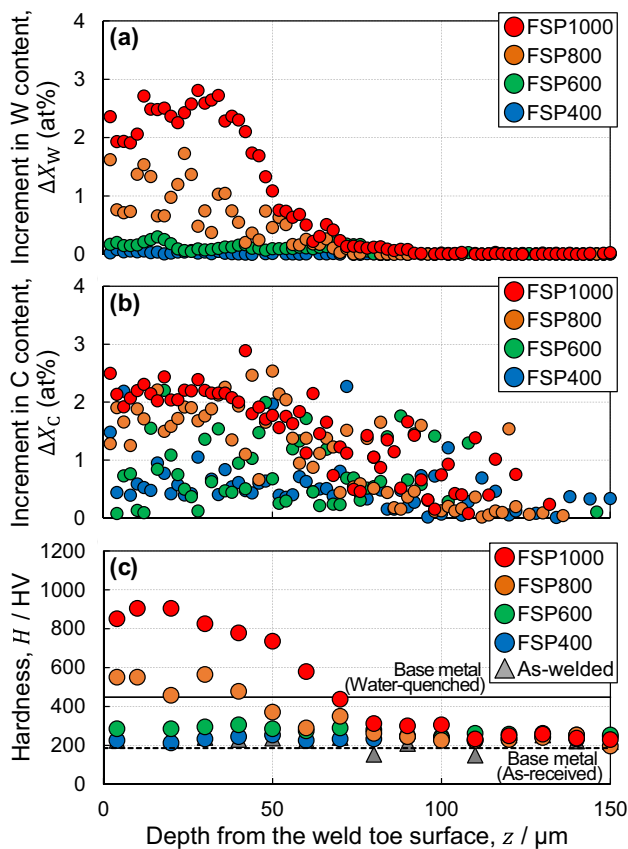


Fig. 4 Variation of increment in (a) W and (b) C contents and (c) hardness with depth from the surface in the topmost layer of weld toes for as-welded joints with and without FSP, depending on tool rotational speed

with hardening the outermost surface layer in comparison with hardening due to grain refinement. The increment was concentrated beneath the surface and the segregated depth was about 50 μm in W and 100 μm in C (Fig. 4(a), (b)). The W and C concentrated depth varied with a diffusion length in the steel austenitized during FSP; the C atoms with smaller radius can diffuse more easily than the W atoms. The increment of W and C contents increased with increasing tool rotational speed and was estimated to be about 2.36 and 2.17 at%, respectively, in sample FSP1000. It suggests that increasing tool rotation speed accelerates the tool wear during FSP and provides larger amounts of W and C to the steel side [31]. The hardness increment in the outermost surface layer with respect to the base metal exhibited similar trend of increment in W content in each specimen (Fig. 4(c)). The increment was small in FSP400 and FSP600, and increased with increasing tool rotational speed in FSP800 and FSP1000. Note that the hardness increment due to W and C solid solution hardening was larger than that due to grain refinement (see FSP400 and FSP600). The average hardness of the outermost surface layer was 552 and 878 HV, respectively, in FSP800 and FSP1000, and was higher than that of the water-quenched base metal (449 HV) consisting of fully martensite structure.

To further characterize the distribution of tool constituent elements in the outermost surface layer, TEM-EDS analyses were conducted for the thin film specimens taken from the weld toe surfaces (Fig. 3(j)–(l)). Figure 5 shows TEM-EDS results obtained in samples FSP600, FSP800, and FSP1000. Polygonal ferrite grains about a few micrometers in average diameter were observed in the outermost surface layer of the weld toe in FSP600, as shown in the TEM-bright field (BF) images (Fig. 5(a), (b)). W segregation was hardly observed in any ferrite grains or at their boundaries in the EDS-W map image (Fig. 5(c)). On the other hand, grain structure in the outermost surface layer of the weld toes in FSP800 and FSP1000 (Fig. 5(d), (g)) became finer than that in FSP600 (Fig. 5(a)). Enlarged images showed obvious change in grain morphology, and the layer included fine elongated grains (Fig. 5(e), (h)). The EDS-W map images (Fig. 5(f), (i)) exhibited higher homogeneously distributed W content than that in FSP600 (Fig. 5(c)). In addition, a few W-rich particles were observed in FSP1000 (Fig. 5(i)).

To identify W content in the outermost layer, EDS quantitative analyses were conducted at points A–I in the steel matrix in Fig. 5(b), (e), and (h) and at points 1–3 in the W-rich particles in Fig. 5(g), indicated by red and yellow arrows, respectively. A summary is presented in Table 3. The average W contents obtained in the steel matrix of samples FSP600, FSP800, and FSP1000 based on the TEM-EDS analyses were estimated to be 0.11, 1.43, and 2.25 at%, in good agreement with those obtained using a 5- μm -diameter

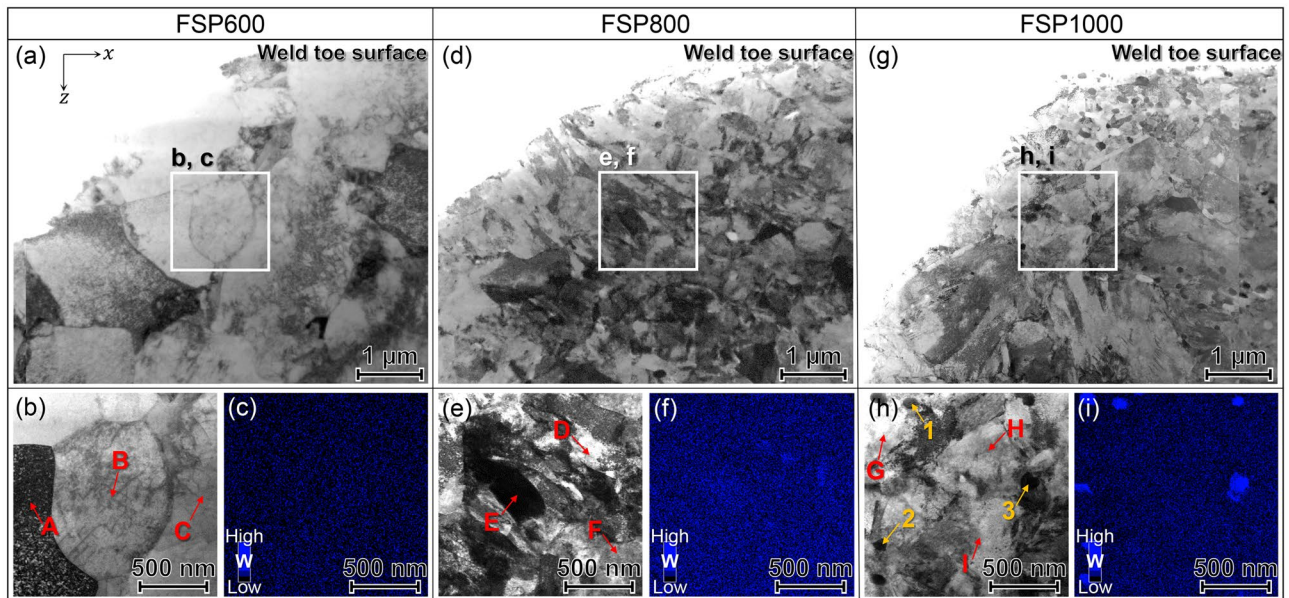


Fig. 5 TEM-BF and EDS-W map images obtained from the outermost surface layer in weld toes for samples (a–c) FSP600, (d–f) FSP800, and (g–i) FSP1000

electron-beam spot using EPMA (Fig. 4(a)), suggesting that the tool constituent W atoms were homogeneously distributed in the topmost steel matrix layer after FSP. On the other hand, the W-rich particles observed in FSP1000 exhibited average W content of 23.42 at%, suggesting that the particle could be an embedded $\text{Fe}_4\text{W}_2\text{C}$ fragment that had dropped out of the WC tool tip and was milled at the interface between the tool and steel surface. $\text{Fe}_4\text{W}_2\text{C}$ particles were reported to form at the tool tip as result of reaction of a WC particle with Fe atoms diffused from the steel matrix [31], together with decomposition of most of the fragment

Table 3 W contents obtained at points A–I and 1–3 in Fig. 5 indicated by red and yellow arrows in the steel matrices and particles, respectively, based on EDS quantitative analyses

Code	Measuring point	W content, X_W (at%)	Average
FSP600	Matrix	A	0.11
		B	
		C	
FSP800	Matrix	D	1.43
		E	
		F	
		G	
FSP1000	Matrix	H	23.42
		I	
	Particle	1	
		2	
		3	

into W and C atoms during milling at the interface under high temperature and pressure due to FSP friction. Most of the tool constituent elements seem to have dissolved in the outermost surface layer of steel matrix austenitized around the peak temperatures during FSP, followed by martensitic transformation during cooling, resulting in fine martensite laths in the outermost surface layer (Fig. 5(e), (h)). Note that the solid-soluble W and C contents in the α -Fe phase were almost zero at room temperature. The hardness of the topmost layer was significantly higher than that of the water-quenched base metal. This can be explained by solid solution hardening due to the supersaturated W and C atoms (WC tool constituent elements). The hardening is associated with large lattice distortion caused by substitutional solid solution of the extra W into the martensite as well as interstitial solid solution of the extra C. The higher solid solute W contents could contribute to the higher increase in hardness in FSP1000. The W-rich particles cannot have effectively increased the hardness, since their size of about 100 nm was too large to impede the movement of dislocations.

3.2 Fatigue strength of welded joints with FSP depending on tool rotational speed

Fatigue strength of weld toes with the FSP-modified topmost layer was investigated. The FSP-modified topmost layer was alloyed with WC tool constituent elements together with grain refinement. Their applied nominal stress amplitude dependence on number of cycles to failure (S–N diagram) is shown in Fig. 6, together with those of an as-welded joint

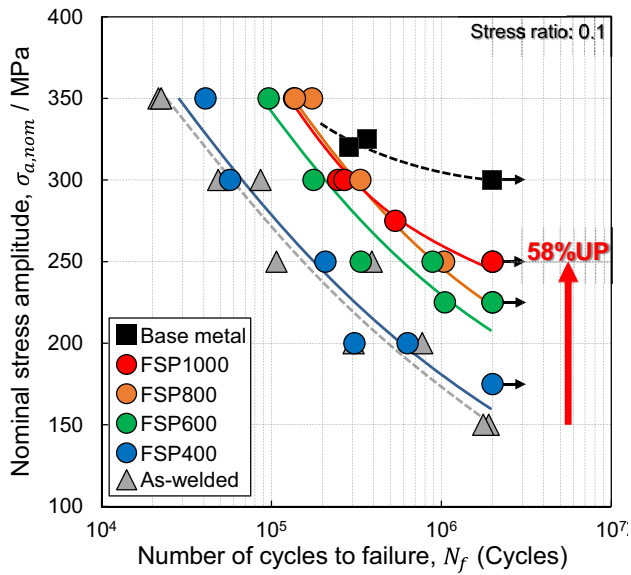


Fig. 6 S–N diagram obtained in four-point bending fatigue tests for samples FSP400, FSP600, FSP800, and FSP1000, together with those for an as-welded joint and a base metal

and a base metal. Since the specimens did not fail up to 2×10^6 cycles (shown with additional arrows on symbols), this number was defined as the fatigue limit. The other joint specimens failed due to local stress concentration at the weld toe. The nominal stress amplitude of the joint specimens subjected to FSP increased with increasing tool rotational speed, and the values at 2×10^6 cycles were estimated from the S–N curves to be about 164, 214, 223, and 248 MPa in samples FSP400, FSP600, FSP800, and FSP1000, respectively. The nominal stress amplitude at 2×10^6 cycles in FSP1000 increased by 58% in comparison to that in the as-welded joint. On the other hand, it was still much lower than that of the base metal. All the joint specimens with and without FSP had the excess weld metal, while the base metal specimens had a flat surface polished for removing stress concentration sources. The joint specimens failed due to local stress concentration at the weld toe and exhibited lower

fatigue limit than that of the base metal. The effect of local stress concentration on fatigue strength is discussed below.

To understand the difference in nominal stress amplitude between these joints, stress concentration effects related to the weld toe geometry were investigated. The elastic stress concentration factor of k_t and fatigue notch factor of k_f for the butt-welded joints under the bending load were calculated from Eqs. (1) and (2), below, respectively [32]:

$$k_t = 1 + 0.165(\tan\theta)^{1/6}(t/r)^{1/2} \tag{1}$$

$$k_f = 1 + (k_t - 1)/(1 + a/r) \tag{2}$$

where t is the plate thickness of 10 mm and θ and r are the weld toe angle and radius, respectively, measured in Figs. 2(b) and 3(a)–(d). Peterson’s material parameter of a for steels is obtained from Eq. (3) [32]:

$$a = 1.087 \times 10^5 \sigma_{uts}^{-2} \tag{3}$$

where σ_{uts} is the ultimate tensile strength of the weld toe, obtained using the small tensile specimens. The values of k_t and k_f calculated in all the joints with and without FSP are summarized in Table 4, together with t , θ , r , and σ_{uts} . The k_f values of all butt-welded joints with FSP were similar and reduced by about 10% due to the significant increase in the weld toe radius, compared to that of the as-welded joint.

The local stress amplitude [33] as fatigue strength at the weld toe of $\sigma_{w,loc}$ was calculated from Eq. (4):

$$\sigma_{w,loc} = \sigma_{w,nom} \cdot k_f \tag{4}$$

where the nominal stress amplitude of $\sigma_{w,nom}$ was defined as that at 2×10^6 cycles in Fig. 6. Note that the $\sigma_{w,loc}$ is associated with effects of factors other than the weld toe geometry modification, such as microstructure and surface roughness modification. Figure 7 shows relationship between the calculated $\sigma_{w,loc}$ and $\sigma_{w,nom}$ for all the joints with FSP variation with tool rotational speed, together with the $\sigma_{w,nom}$ and $\sigma_{w,loc}$ of the as-welded joint and the $\sigma_{w,nom}$ of the base metal. The $\sigma_{w,loc}$ in sample FSP400 was lower than that in the as-welded

Table 4 Weld toe parameters for the as-welded joint, FSP400, FSP600, FSP800, and FSP1000

Code	Plate thickness, t (mm)	Weld toe angle, θ (°)	Weld toe radius, r (mm)	Ultimate tensile strength of the weld toe, σ_{uts} (MPa)	Elastic stress concentration factor, k_t	Fatigue notch factor, k_f
As-welded	10	27	0.27	555	1.90	1.39
FSP400		40	3.69	637	1.26	1.25
FSP600		32	2.65	655	1.30	1.27
FSP800		36	3.53	672	1.26	1.25
FSP1000		33	3.60	707	1.26	1.24

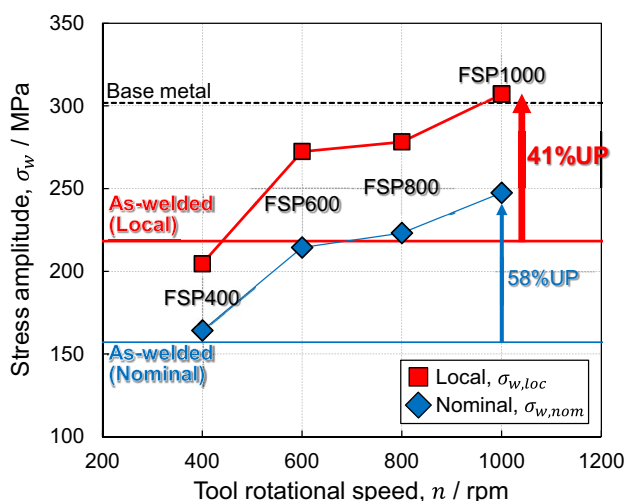


Fig. 7 Nominal and local stress amplitude variation with tool rotational speed in samples FSP400, FSP600, FSP800, and FSP1000

joint, even though the weld toe microstructure was significantly refined. This can be associated with the notched surface because of low heat input (Fig. 3(e)). On the other hand, values of the $\sigma_{w,loc}$ in FSP600, FSP800, and FSP1000 with the smooth weld toe surface were obviously higher than that of the as-welded joint. Especially, the value of the $\sigma_{w,loc}$ in FSP1000 was about 41% higher than that of the as-welded joint. This indicates that microstructure modification in the topmost layer of weld toes provided much larger increase

in fatigue strength than the weld toe geometry modification. Increase of $\sigma_{w,loc}$ in FSP600 can be explained by grain refinement. Those in FSP800 and FSP1000 were a little higher and much higher, respectively, than that in FSP600. The further increase in FSP800 and FSP1000 is associated with the alloying of the topmost layer of weld toes with the tool constituent elements. The alloying led to W and C solid solution hardening together with the related martensitic transformation.

To clarify the effect of the alloyed topmost layer on the fatigue strength increase observed in samples FSP800 and FSP1000, fracture surface observation and analysis were performed. Figure 8 shows SEM images of fracture surfaces obtained after fatigue failure at stress amplitude of 300 MPa for all the joints with and without FSP. The observed fracture surfaces can be divided into two regions, consisting of flat surface caused by fatigue crack initiation and propagation and rough surface corresponding to the fast fracture region. Many ratchet marks (white arrows), forming a boundary between two adjacent failure planes, were observed on the fracture surfaces beneath the weld toe surface. The more crack initiation sites there were, the more ratchet marks were present. The average number of ratchet marks per unit length on the fracture surfaces for all the joints is shown in Fig. 9. The average value in FSP400 was more than that in the as-welded joint. The enlarged crack initiation region beneath the weld toe surface showed rough, discontinuous, brittle fracture planes (Fig. 8(c)). The crack initiation occurred at the notch bottom in the rough surface after FSP (Fig. 3(e)),

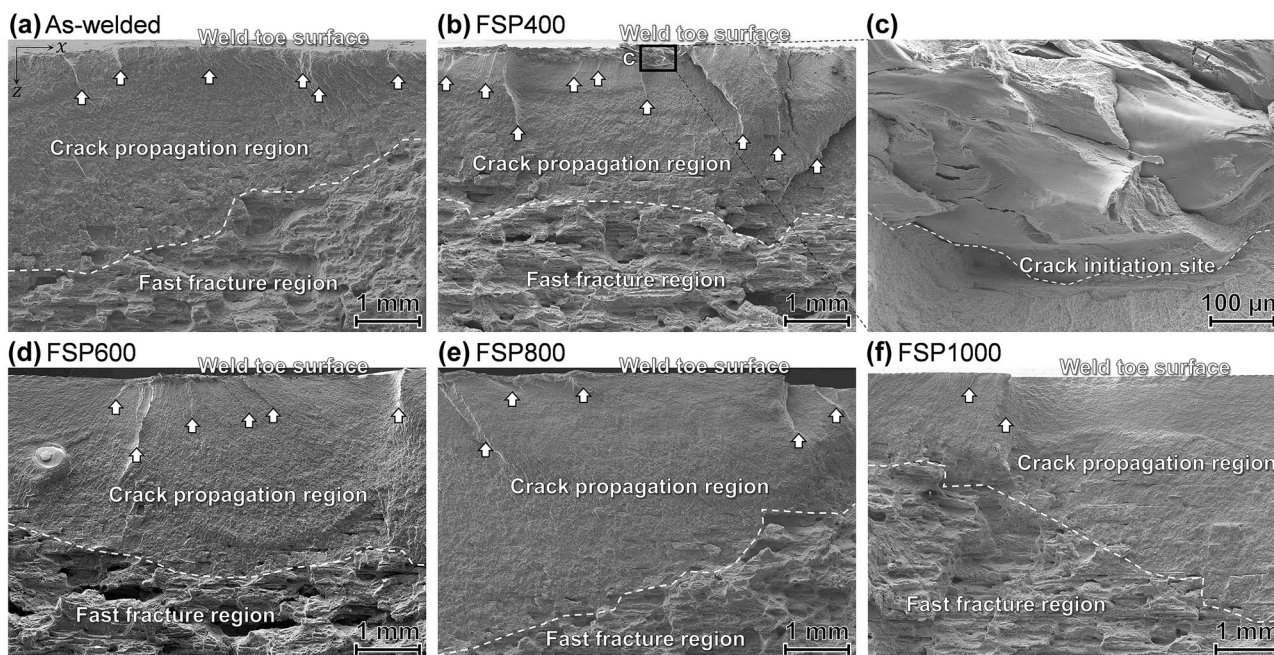


Fig. 8 SEM images of the fracture surface obtained after fatigue failure at stress amplitude of 300 MPa for the (a) as-welded joint, (b) and (c) FSP400, (d) FSP600, (e) FSP800, and (f) FSP1000

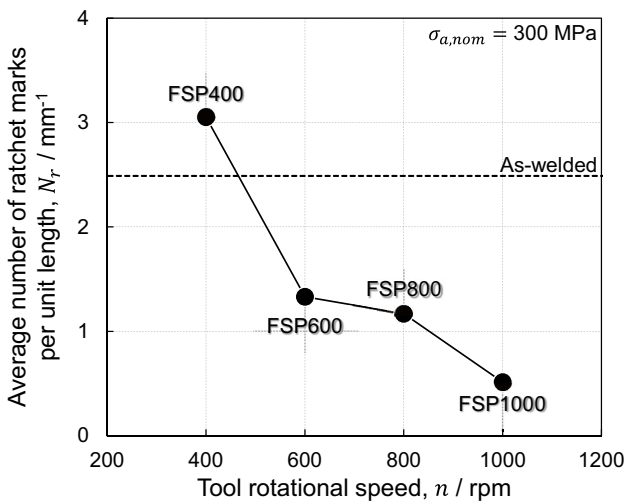


Fig. 9 Average number of ratchet marks per unit length on fracture surfaces after fatigue failure at stress amplitude of 300 MPa in the as-welded joint, FSP400, FSP600, FSP800, and FSP1000

resulting in the lower $\sigma_{w,loc}$ in FSP400 than that in the as-welded joint. On the other hand, the fatigue fracture surface in FSP600, FSP800, and FSP1000 was smoother and had much fewer ratchet marks than in the as-welded joint and FSP400. The average number of ratchet marks per unit length on the fracture surfaces in FSP600, FSP800, and FSP1000 decreased with increasing tool rotational speed. This suggests that resistance to crack initiation at the weld

toe surface during fatigue tests can be enhanced by increasing hardness due to solid solution hardening, by alloying the topmost layer with W and C elements.

To understand the effect of the alloyed topmost layer on increase in the fatigue strength, the fatigue failure position and distributions of the alloyed tool constituent elements near the failure position were investigated. Figure 10 shows cross-sectional OM and EPMA-W map images obtained near the fatigue failure at the stress amplitude of 300 MPa in samples FSP800 and FSP1000. Both the EPMA-W map images indicate that the fatigue failure occurred at the surface position without the tool constituent elements. This suggests that alloying the weld toe surface with tool constituent elements increased resistance to fatigue crack initiation, and the crack initiated at the excess weld metal with higher thickness than that in the base metal. Especially, the increment of the alloyed W and C contents near the weld toe surface in FSP1000 was the highest, resulting in the highest hardness, leading to the largest increase in fatigue strength among all the joints with FSP-modified weld toes. The increment of the alloyed W and C contents is associated with WC tool wear during FSP, and increment of both the W and C contents and WC tool wear increased with increasing tool rotational speed [31]. The tool wear has been considered as an unavoidable issue in high-strength materials during FSP, but these results indicate that alloying the weld toe with tool constituent elements could be an effective technique for increasing fatigue strength of welded steel joints.

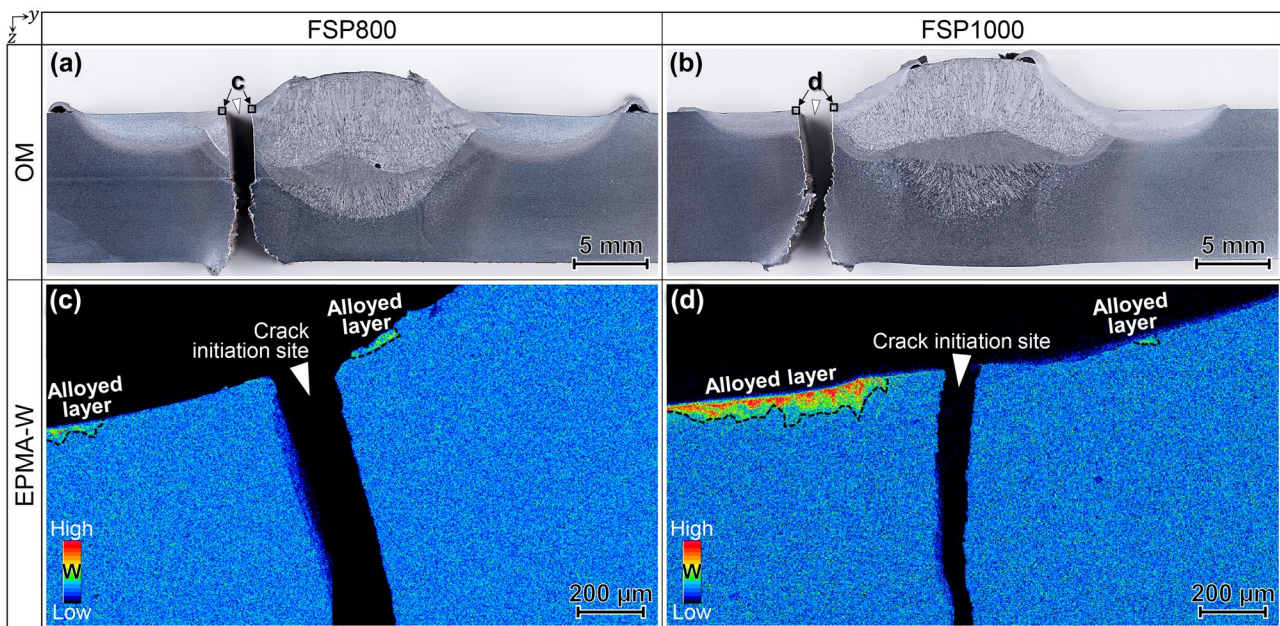


Fig. 10 (a and b) Cross-sectional OM images of samples FSP800 and FSP1000 after fatigue failure at stress amplitude of 300 MPa and (c and d) EPMA-W map images obtained at the enlarged areas c in (a) and d in (b), respectively

4 Conclusions

To clarify influence of the tool rotational speed on increasing fatigue strength, FSP was conducted on the weld toes of HSLA steel joints with various rotational speeds of 400, 600, 800, and 1000 rpm. Alloying of the topmost steel layer with WC tool constituent elements of W and C occurred at high rotational speeds together with occurrence of WC tool wear at the SZ surface. Solid solution hardening increased hardness at the topmost steel layer, and the hardness increased with increasing tool rotational speed. This led to increase in fatigue strength and resulted in the maximum increase obtained in sample FSP1000. The important findings are as follows:

- 1) The average hardness of the topmost steel layer was 552 and 878 HV in samples FSP800 and FSP1000, respectively. These values were higher than hardness of the water-quenched base metal. The higher hardness was caused by solid solution hardening due to the supersaturated W and C in the topmost layer, which contained martensite laths. In contrast, hardness increases in the topmost layer of FSP400 and FSP600 were caused by grain refinement only.
- 2) The nominal stress amplitude increased with increasing tool rotational speed, and the values at 2×10^6 cycles (fatigue limit) were estimated to be about 164, 214, 223, and 248 MPa in samples FSP400, FSP600, FSP800, and FSP1000, respectively. The maximum value in FSP1000 was 58% higher than that in the as-welded joint.
- 3) The $\sigma_{w,loc}$ in sample FSP400 was lower, while those in FSP600, FSP800, and FSP1000 were obviously higher than that in the as-welded joint. The lower $\sigma_{w,loc}$ in FSP400 could be associated with the notched surface. Increase of $\sigma_{w,loc}$ in FSP600 can be explained by grain refinement. Those in FSP800 and FSP1000 were a little higher and much higher, respectively, than that in FSP600. This could be associated with the alloying of the topmost layer of the weld toes with the tool constituent elements. The alloying led to W and C solid solution hardening together with the related martensitic transformation.
- 4) The number of ratchet marks on the fatigue fracture surface was reduced by increasing tool rotational speed, indicating reduction of crack initiation sites. The crack tended to initiate at a weld toe surface that corresponded to the end of or a little apart from the alloyed area containing the tool constituent elements. This suggests that the W and C solid solution hardening prevented fatigue crack initiation.

Author contribution Hajime Yamamoto: conceptualization, methodology, validation, investigation, data curation, writing — original draft, and visualization. Shodai Koga: investigation, data curation, and visualization. Kazuhiro Ito: conceptualization, writing — review and editing, and supervision. Yoshiki Mikami: methodology.

Funding This work was supported by JSPS KAKENHI Grant Number JP19K23575 and a future pioneering project commissioned by the New Energy and Industrial Technology Development Organization (NEDO).

Data availability The data presented in this study are available from the corresponding author upon reasonable request.

Declarations

Ethics approval and consent to participate Not applicable.

Consent for publication Authors consent to publish this article.

Competing interests The authors declare no competing interests.

Open Access This article is licensed under a Creative Commons Attribution 4.0 International License, which permits use, sharing, adaptation, distribution and reproduction in any medium or format, as long as you give appropriate credit to the original author(s) and the source, provide a link to the Creative Commons licence, and indicate if changes were made. The images or other third party material in this article are included in the article's Creative Commons licence, unless indicated otherwise in a credit line to the material. If material is not included in the article's Creative Commons licence and your intended use is not permitted by statutory regulation or exceeds the permitted use, you will need to obtain permission directly from the copyright holder. To view a copy of this licence, visit <http://creativecommons.org/licenses/by/4.0/>.

References

1. Fueki R, Takahashi K, Handa M (2019) Fatigue limit improvement and rendering defects harmless by needle peening for high tensile steel welded joint. *Met* 9:143. <https://doi.org/10.3390/met9020143>
2. Lago J, Trško L, Jambor M, Nový F, Bokůvka O, Mičian M, Pastorek F (2019) Fatigue life improvement of the high strength steel welded joints by ultrasonic impact peening. *Met* 9:619. <https://doi.org/10.3390/met9060619>
3. Hensel J, Eslami H, Nitschke-Pagel T, Dilger K (2019) Fatigue strength enhancement of butt welds by means of shot peening and clean blasting. *Met* 9:744. <https://doi.org/10.3390/met9070744>
4. Fueki R, Takahashi K (2021) Improving the fatigue limit and rendering a defect harmless by laser peening for a high strength steel welded joint. *Opt Laser Technol* 134:106605. <https://doi.org/10.1016/j.optlastec.2020.106605>
5. Kang HT, Lee Y-L, Sun XJ (2008) Effects of residual stress and heat treatment on fatigue strength of weldments. *Mater Sci Eng A* 497:37–43. <https://doi.org/10.1016/j.msea.2008.06.011>
6. Aung MP, Katsuda H, Hirohata M (2019) Fatigue-performance improvement of patch-plate welding via PWHT with induction heating. *J Constr Steel Res* 160:280–288. <https://doi.org/10.1016/j.jcsr.2019.05.047>
7. Baptista R, Infante V, Branco CM (2008) Study of the fatigue behavior in welded joints of stainless steels treated by weld toe grinding and subjected to salt water corrosion. *Int J Fatigue* 30:453–462. <https://doi.org/10.1016/j.ijfatigue.2007.04.011>
8. Fu Z, Ji B, Kong X, Chen X (2017) Grinding treatment effect on rib-to-roof weld fatigue performance of steel bridge decks. *J Const Steel Res* 129:163–170. <https://doi.org/10.1016/j.jcsr.2016.09.018>

9. Kim I-T, Kim H-S, Dao DK, Ahn J-H, Jeong Y-S (2018) Fatigue resistance improvement of welded joints by bristle roll-brush grinding. *Int J Steel Struct* 18:1631–1638. <https://doi.org/10.1007/s13296-018-0059-1>
10. Dahle T (1998) Design fatigue strength of TIG-dressed welded joints in high-strength steels subjected to spectrum loading. *Int J Fatigue* 20:677–681. [https://doi.org/10.1016/S0142-1123\(98\)00031-0](https://doi.org/10.1016/S0142-1123(98)00031-0)
11. Ramalho AL, Ferreira JAM, Branco CAGM (2011) Fatigue behaviour of T welded joints rehabilitated by tungsten inert gas and plasma dressing. *Mater Des* 32:4705–4713. <https://doi.org/10.1016/j.matdes.2011.06.051>
12. Skriko T, Ghafouri M, Björk T (2017) Fatigue strength of TIG-dressed ultra-high-strength steel fillet weld joints at high stress ratio. *Int J Fatigue* 94:110–120. <https://doi.org/10.1016/j.ijfatigue.2016.09.018>
13. Yıldırım HC (2017) Recent results on fatigue strength improvement of high-strength steel welded joints. *Int J Fatigue* 101:408–420. <https://doi.org/10.1016/j.ijfatigue.2016.10.026>
14. Ito K, Okuda T, Ueji R, Fujii H, Shiga C (2014) Increase of bending fatigue resistance for tungsten inert gas welded SS400 steel plates using friction stir processing. *Mater Des* 61:275–280. <https://doi.org/10.1016/j.matdes.2014.04.076>
15. Yamamoto H, Ito K (2018) Effects of microstructural modification using friction stir processing on fatigue strength of butt-welded joints for high-strength steels. *Mater Sci Appl* 9:625–636. <https://doi.org/10.4236/msa.2018.97045>
16. Yamamoto H, Danno Y, Ito K, Mikami Y, Kohama K, Fujii H (2018) Application of friction stir processing to weld toe for fatigue strength improvement of high-strength low-alloy steel joint. *Weld Lett* 36:1WL–4WL. <https://doi.org/10.2207/qjws.36.1WL>
17. Yamamoto H, Danno Y, Ito K, Mikami Y, Fujii H (2018) Weld toe modification using spherical-tip WC tool FSP in fatigue strength improvement of high-strength low-alloy steel joints. *Mater Des* 160:1019–1028. <https://doi.org/10.1016/j.matdes.2018.10.036>
18. Yamamoto H, Nishiura T, Nishibata H, Yonemura M, Fujiwara K, Kawano K, Ito K (2020) Surface microstructure modifications of low carbon steel welds produced by low-heat-input friction stir processing. *Mater Trans* 61:1613–1619. <https://doi.org/10.2320/matertrans.MT-M2020117>
19. Mishra RS, Ma ZY (2005) Friction stir welding and processing. *Mater Sci Eng R* 50:1–78. <https://doi.org/10.1016/j.mser.2005.07.001>
20. Yadav D, Bauri R (2012) Effect of friction stir processing on microstructure and mechanical properties of aluminium. *Mater Sci Eng A* 539:85–92. <https://doi.org/10.1016/j.msea.2012.01.055>
21. Sekban DM, Aktarer SM, Xue P, Ma ZY, Purcek G (2016) Impact toughness of friction stir processed low carbon steel used in ship-building. *Mater Sci Eng A* 672:40–48. <https://doi.org/10.1016/j.msea.2016.06.063>
22. Xue P, Wang BB, Chen FF, Wang WG, Xiao BL, Ma ZY (2016) Microstructure and mechanical properties of friction stir processed Cu with an ideal ultrafine-grained structure. *Mater Charact* 121:187–194. <https://doi.org/10.1016/j.matchar.2016.10.009>
23. Luo XC, Kang LM, Liu HL, Li ZJ, Liu YF, Zhang DT, Chen DL (2020) Enhancing mechanical properties of AZ61 magnesium alloy via friction stir processing: effect of processing parameters. *Mater Sci Eng A* 797:139945. <https://doi.org/10.1016/j.msea.2020.139945>
24. Ni DR, Wang D, Feng AH, Yao G, Ma ZY (2009) Enhancing the high-cycle fatigue strength of Mg–9Al–1Zn casting by friction stir processing. *Scr Mater* 61:568–571. <https://doi.org/10.1016/j.scriptamat.2009.05.023>
25. Jana S, Mishra RS, Baumann JB, Grant G (2010) Effect of friction stir processing on fatigue behavior of an investment cast Al–7Si–0.6 Mg alloy. *Acta Mater* 58:989–1003. <https://doi.org/10.1016/j.actamat.2009.10.015>
26. Kapoor R, Kandasamy K, Mishra RS, Baumann JA, Grant G (2013) Effect of friction stir processing on the tensile and fatigue behavior of a cast A206 alloy. *Mater Sci Eng A* 561:159–166. <https://doi.org/10.1016/j.msea.2012.10.090>
27. da Silva J, Costa JM, Loureiro A, Ferreira JM (2013) Fatigue behaviour of AA6082-T6 MIG welded butt joints improved by friction stir processing. *Mater Des* 51:315–322. <https://doi.org/10.1016/j.matdes.2013.04.026>
28. Borrego LP, Costa JD, Jesus JS, Loureiro AR, Ferreira JM (2014) Fatigue life improvement by friction stir processing of 5083 aluminium alloy MIG butt welds. *Theor Appl Fract Mech* 70:68–74. <https://doi.org/10.1016/j.tafmec.2014.02.002>
29. Costa JDM, Jesus JS, Loureiro A, Ferreira JAM, Borrego LP (2014) Fatigue life improvement of MIG welded aluminium T-joints by friction stir processing. *Int J Fatigue* 61:244–254. <https://doi.org/10.1016/j.ijfatigue.2013.11.004>
30. Jesus JS, Costa JM, Loureiro A, Ferreira JM (2017) Fatigue strength improvement of GMAW T-welds in AA5083 by friction-stir processing. *Int J Fatigue* 61:124–134. <https://doi.org/10.1016/j.ijfatigue.2016.12.034>
31. Yamamoto H, Imagawa Y, Ito K, Chen K, Zhang L (2021) Alloying a topmost steel-plate layer with WC-tool constituent elements during friction stir processing. *J Manuf Process* 69:311–319. <https://doi.org/10.1016/j.jmapro.2021.07.050>
32. Yung J-Y, Lawren FV (1985) Analytical and graphical aids for the fatigue design of weldments. *Fatigue Fract Eng Mater Struct* 8:223–241. <https://doi.org/10.1111/j.1460-2695.1985.tb00424.x>
33. Hearn EJ (1997) Chapter 10 - Contact stress, residual stress and stress concentrations. In: *Mechanics of materials 2* (3rd edn.) An introduction to the mechanics of elastic and plastic deformation of solids and structural materials, pp. 381–442. <https://doi.org/10.1016/B978-075063266-9/50011-1>

Publisher's Note Springer Nature remains neutral with regard to jurisdictional claims in published maps and institutional affiliations.